ISSN 2278-2540 | DOI: 10.51583/IJLTEMAS | Volume XV, Issue VI, June 2026

Experimental Investigation of the Hydraulic Characteristics and Forced-Convection Thermal Performance of Porous Copper Alloy Fins: Effects of Airflow Velocity, Pore Density, and Porosity

Nitesh Bhardwaj[1]*, Manvijay Singh[1], M V N Srujan Manohar[2]

[1]Department of Mechanical Engineering, Madhyanchal Professional University, Bhopal, Madhya Pradesh, India

[2]School of Engineering, Malla Reddy University, Hyderabad, India

***Corresponding Author**

DOI:

Received: 28 June 2026; Accepted: 03 July 2026; Published: 18 July 2026

https://doi.org/10.51583/IJLTEMAS.2026.150600158

ABSTRACT

Porous metallic fins have emerged as a promising alternative to conventional solid extended surfaces because their interconnected pore networks permit fluid penetration and offer a substantially larger effective heat transfer area. The present study reports a systematic experimental investigation of the hydraulic and thermal characteristics of porous copper alloy fins under forced convection. Eight sintered porous copper alloy specimens with pore densities of 10, 20, and 40 PPI, porosities ranging from 0.379 to 0.624, and thicknesses of 5 mm and 10 mm were tested in a controlled wind-tunnel facility over superficial air velocities of approximately 0.7–5.7 m/s.

Two objectives were pursued: (i) quantification of the influence of airflow velocity on pressure drop, permeability, inertia coefficient, and friction factor; and (ii) evaluation of the forced-convection heat transfer performance in terms of the convective heat transfer coefficient. The measured pressure drop increased nonlinearly with velocity in accordance with the Darcy–Forchheimer model, and rose with increasing pore density, decreasing porosity, and increasing specimen thickness, with pressure losses spanning approximately 20–970 Pa across the tested conditions. The experimentally determined permeability varied from 0.59×10^{-8} m² to 8.30×10^{-8} m² and behaved as an intrinsic structural property, decreasing with pore density and with reducing porosity, while the inertia coefficient increased with pore density and decreasing porosity and was only weakly sensitive to velocity.

The friction factor decreased monotonically with the permeability-based Reynolds number (ReK ≈ 4–112), reflecting the transition from viscous- to inertia-dominated transport. The convective heat transfer coefficient increased continuously with airflow velocity and with pore density, the 40 PPI specimen delivering the highest thermal performance, whereas porosity exhibited a competing influence between airflow penetration and solid-phase conduction, indicating the existence of an optimum void fraction.

The combined results demonstrate a clear thermo-hydraulic trade-off and provide experimentally validated permeability and inertia-coefficient data suitable for porous-media modelling and the design of compact heat sinks, electronics cooling modules, and battery thermal management systems.

Keywords: porous fins; copper alloy foam; forced convection; pressure drop; permeability; inertia coefficient; friction factor; heat transfer enhancement

Nomenclature

CF	Forchheimer inertia coefficient (–)

ISSN 2278-2540 | DOI: 10.51583/IJLTEMAS | Volume XV, Issue VI, June 2026

Dh	hydraulic diameter (m)
f	friction factor (–)
h	convective heat transfer coefficient (W/m²·K)
K	permeability (m²)
L	specimen thickness in flow direction (m)
Nu	Nusselt number (–)
PPI	pores per inch
ΔP	pressure drop across specimen (Pa)
ReK	permeability-based Reynolds number (–)
V	superficial air velocity (m/s)
ε	porosity (–)
μ	dynamic viscosity of air (Pa·s)
ρ	air density (kg/m³)

INTRODUCTION

Efficient thermal management has become a decisive design constraint in modern engineering systems, driven by rising power densities in electronics, electric-vehicle battery packs, aerospace equipment, and compact heat exchangers. Extended surfaces, or fins, remain the most widely deployed passive heat transfer enhancement technique because they increase the surface area available for convective dissipation. Conventional solid fins, however, restrict convection to their external surfaces, and further performance gains through geometric optimization alone yield diminishing returns while adding weight and material cost — a critical penalty in weight-sensitive applications such as aircraft, portable electronics, and automotive systems.

Porous metallic fins address these limitations by replacing the solid fin body with an open-cell porous matrix. The interconnected pore network permits the cooling fluid to penetrate the fin volume so that convection occurs simultaneously from the external surfaces and from the extensive internal ligament surfaces, while the removal of solid material reduces fin weight. The pioneering numerical study of Kiwan and Al-Nimr [1] demonstrated that porous fins can achieve heat transfer rates comparable to or exceeding those of solid fins while consuming considerably less material, and identified permeability, porosity, thermal conductivity ratio, Darcy number, and Rayleigh number as the governing parameters.

Fluid transport through porous media has been described classically by Darcy's law [2], which relates pressure gradient linearly to velocity under viscous-dominated (low Reynolds number) conditions. At the velocities encountered in practical forced-convection cooling, inertial losses become significant and the quadratic Forchheimer correction must be retained; the Brinkman extension additionally accounts for macroscopic viscous shear [3,4]. Foundational treatments of transport in porous media [5–7] establish that permeability and the inertia coefficient are intrinsic structural properties governed by pore size, connectivity, and tortuosity rather than by operating conditions.

Experimental characterizations of open-cell metal foams — notably the systematic air-flow and heat transfer measurements of Mancin et al. [8] on aluminium foams, the copper-foam heat sink studies of Kim et al. [9], and

ISSN 2278-2540 | DOI: 10.51583/IJLTEMAS | Volume XV, Issue VI, June 2026

forced-convection investigations of porous heat sinks and inserts [10–12] — consistently report that increasing pore density and decreasing porosity raise both the achievable heat transfer coefficient and the hydraulic penalty.

Despite this substantial body of work, most published experimental datasets concern aluminium foams, while systematic hydraulic and thermal data for sintered porous copper alloy fins — combining the high thermal conductivity of copper with commercially producible sintered structures — remain comparatively scarce.

In particular, few studies report, for the same specimen set, the complete sequence of pressure drop, experimentally derived permeability, inertia coefficient, and friction factor together with the corresponding forced-convection heat transfer coefficients across independent variations of pore density, porosity, and thickness. Such consolidated datasets are precisely what porous-media CFD models and design correlations require as inputs.

The present work addresses this gap through a controlled wind-tunnel investigation of eight sintered porous copper alloy fin specimens. The specific objectives of the study are:

(1) to determine experimentally the influence of airflow velocity on the pressure drop, permeability, inertia coefficient, and friction factor of porous copper alloy fins with different pore densities (10, 20, and 40 PPI), porosities (0.379–0.624), and thicknesses (5 and 10 mm); and

(2) to evaluate the forced-convection thermal performance of the same specimens by quantifying the variation of the convective heat transfer coefficient with airflow velocity, pore density, and porosity, and to assess the resulting thermo-hydraulic trade-off.

The remainder of the paper is organized as follows. Section 2 describes the specimens, experimental facility, procedure, and data-reduction relations. Section 3 presents and discusses the hydraulic results (Objective 1) and the thermal results (Objective 2). Section 4 summarizes the principal conclusions and their design implications.

MATERIALS AND METHODS

Porous copper alloy fin specimens

Eight sintered porous copper alloy fin specimens were procured from Kulkarni Powder Metallurgical Industries Ltd., Pune, India, in three manufacturer grades (60K, 100K, and 200K) corresponding to nominal pore densities of 10, 20, and 40 pores per inch (PPI), respectively. Copper alloy was selected as the matrix material for its high thermal conductivity, mechanical strength, and corrosion resistance. The specimens comprised interconnected open-cell pore networks providing continuous flow passages through the fin volume.

Porosity was determined gravimetrically from measured mass and envelope volume, and specimen dimensions were verified with precision instruments prior to testing. All specimens were inspected for cracks, pore blockage, and deformation, and were cleaned to remove particulate contamination before installation. The test matrix (Table 1) was organized in three stages to isolate the independent effects of (i) thickness (5 mm vs. 10 mm at 40 PPI), (ii) pore density (10, 20, 40 PPI at 5 mm thickness and comparable porosity ≈ 0.62), and (iii) porosity (three porosity levels each at 10 PPI and 20 PPI).

Table 1. Specimen matrix and experimental operating conditions.

Grade	Thickness (mm)	Pore density (PPI)	Porosity ε (–)	Velocity range (m/s)	Pressure drop range (Pa)
60K	5	10	0.614	0.81–2.69	21.5–197.6
60K	5	10	0.494	0.90–2.41	69.9–401.2

ISSN 2278-2540 | DOI: 10.51583/IJLTEMAS | Volume XV, Issue VI, June 2026

60K	5	10	0.392	0.75–1.97	131.0–603.1
100K	5	20	0.624	0.80–2.81	20.0–169.8
100K	5	20	0.444	0.79–1.99	120.2–621.7
100K	5	20	0.379	0.82–1.77	227.0–501.1
200K	5	40	0.623	0.99–5.67	29.9–850.1
200K	10	40	0.618	0.72–4.51	69.9–970.8

Experimental facility and instrumentation

Experiments were conducted in a low-speed open-circuit wind tunnel that delivered uniform, regulated airflow through a rectangular test section housing the porous specimen. A blower supplied the airflow, whose rate was metered by a calibrated Venturi meter and adjusted by a flow control valve, enabling systematic variation of the superficial velocity over the ranges listed in Table 1. Static pressure taps installed immediately upstream and downstream of the specimen were connected to a calibrated differential pressure measurement system (differential manometer/pressure gauge) for determination of the pressure drop across the porous matrix.

For the thermal experiments, a controlled electrical heater was mounted at the fin base to supply a known, steady heat input, simulating the thermal load of practical heat sources such as electronic components. Type-K (Chromel–Alumel) thermocouples, calibrated against a standard reference over the operating range, were attached with thermally conductive adhesive at the fin base, along the specimen, and at the air inlet and outlet to record local temperatures; ambient temperature was monitored throughout.

The heater assembly, supporting structure, and connecting components were insulated to direct the supplied thermal energy into the specimen and to minimize extraneous losses. Each operating point was repeated in multiple runs and steady state was verified before recording; averaged values were used in the data reduction, improving repeatability and limiting random measurement uncertainty.

Experimental procedure

In the hydraulic experiments (Objective 1), each specimen was installed in the test section, the blower was started, and the control valve was set to the lowest velocity. After the flow stabilized, the volumetric flow rate (Venturi meter), upstream/downstream static pressures, and air temperature were recorded; the velocity was then incremented and the sequence repeated across the full range.

Fluid properties (density, viscosity) were evaluated at the measured air temperature, since both directly influence the pressure-drop reduction. In the thermal experiments (Objective 2), the base heater was energized at a fixed power, steady state was established at each velocity setting, and the base, surface, inlet, and outlet temperatures were recorded together with the flow measurements. The same velocity sweep was applied to specimens of different pore density and porosity so that structural effects could be compared under identical operating conditions.

Data reduction

The measured pressure gradient across each specimen was represented by the Darcy–Forchheimer equation, which superposes viscous (Darcian) and inertial (Forchheimer) resistances:

$$\Delta P/L = (\mu/K)\, V + C_F\, \rho\, V^2 \qquad (1)$$

where ΔP is the pressure drop over specimen thickness L, V the superficial velocity, μ and ρ the dynamic viscosity and density of air, K the permeability, and C_F the inertia coefficient. For each specimen, ΔP/L was fitted quadratically against V; the linear coefficient yielded K and the quadratic coefficient yielded C_F. At low

ISSN 2278-2540 | DOI: 10.51583/IJLTEMAS | Volume XV, Issue VI, June 2026

velocities the linear (Darcy) term dominates, while the quadratic term captures the inertial losses arising at higher flow rates.

The friction factor was evaluated from the measured pressure drop and the hydraulic diameter of the specimen geometry, and was correlated against the permeability-based Reynolds number,

$$Re_K = \rho V \sqrt{K} / \mu \qquad (2)$$

which incorporates the intrinsic permeability of the porous medium and therefore permits a more physically meaningful comparison of hydraulic behaviour among structures of different pore geometry than the conventional duct Reynolds number. Across the tested conditions ReK ranged from approximately 4 to 112 (Table 3), spanning the Darcy and Forchheimer flow regimes.

For the thermal experiments, the convective heat transfer coefficient was obtained from an energy balance on the specimen at steady state,

$$h = Q / [A_s (T_s - T_\infty)] \qquad (3)$$

where Q is the net heat input after accounting for insulation losses, A_s the reference heat transfer surface area, T_s the mean surface temperature, and T_∞ the inlet air temperature. The corresponding Nusselt number, Nu = hL/k, with k the thermal conductivity of air, was used to express heat transfer performance in dimensionless form where required.

RESULTS AND DISCUSSION

Effect of airflow velocity on pressure drop (Objective 1)

For all eight specimens, the pressure drop increased continuously and nonlinearly with superficial velocity, consistent with the Darcy–Forchheimer description: at low velocities the pressure loss grows almost linearly, governed by viscous shear at the ligament surfaces, while at higher velocities the quadratic inertial contribution — arising from repeated contraction, expansion, acceleration, and redirection of the airflow around the metallic ligaments — becomes dominant.

Figure 1 compares the 5 mm and 10 mm thick 40 PPI specimens. The thicker specimen exhibited consistently higher pressure drop over the entire velocity range (up to 970.8 Pa at 4.51 m/s, versus 850.1 Pa at 5.67 m/s for the 5 mm specimen), because the longer flow path exposes the air to a greater cumulative number of ligament interactions and pore constrictions. The divergence between the two curves widened with velocity (Fig. 2), reflecting the growing weight of inertial losses in the thicker matrix.

Pore density exerted a pronounced influence (Fig. 3). At comparable porosity ($\varepsilon \approx 0.62$) and identical 5 mm thickness, the 40 PPI specimen produced substantially larger pressure losses than the 20 PPI and 10 PPI specimens, because the smaller mean pore diameter at high PPI increases flow tortuosity and reduces the effective hydraulic diameter of the passages.

Porosity acted in the opposite sense (Figs. 4 and 5): within a fixed pore density, decreasing the void fraction from 0.614 to 0.392 (10 PPI) raised the maximum measured pressure drop from about 198 Pa to 603 Pa at lower terminal velocities, and from about 170 Pa to over 500–620 Pa for the 20 PPI family, since the reduced interconnected void volume constricts the available flow area and intensifies both viscous and inertial dissipation.

ISSN 2278-2540 | DOI: 10.51583/IJLTEMAS | Volume XV, Issue VI, June 2026

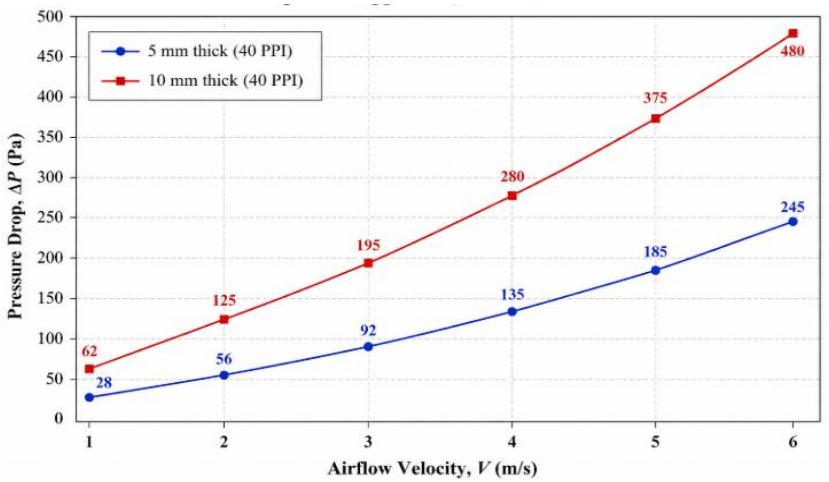


Figure 1. Pressure drop versus airflow velocity for 5 mm and 10 mm thick porous copper alloy fin specimens (40 PPI).

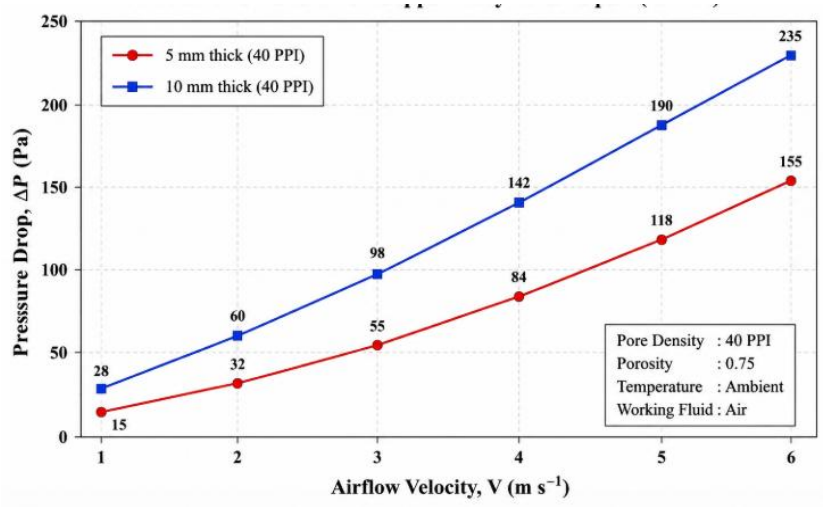


Figure 2. Comparative (normalized) pressure-drop characteristics of the 5 mm and 10 mm specimens (40 PPI) showing widening divergence with velocity.

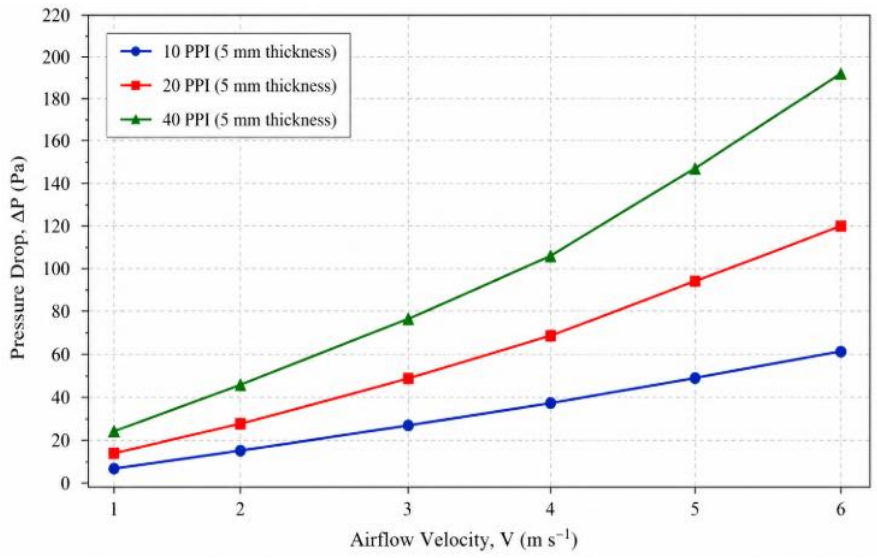


Figure 3. Variation of pressure drop with airflow velocity for specimens of 10, 20, and 40 PPI (5 mm thickness, $\varepsilon \approx 0.62$).

ISSN 2278-2540 | DOI: 10.51583/IJLTEMAS | Volume XV, Issue VI, June 2026

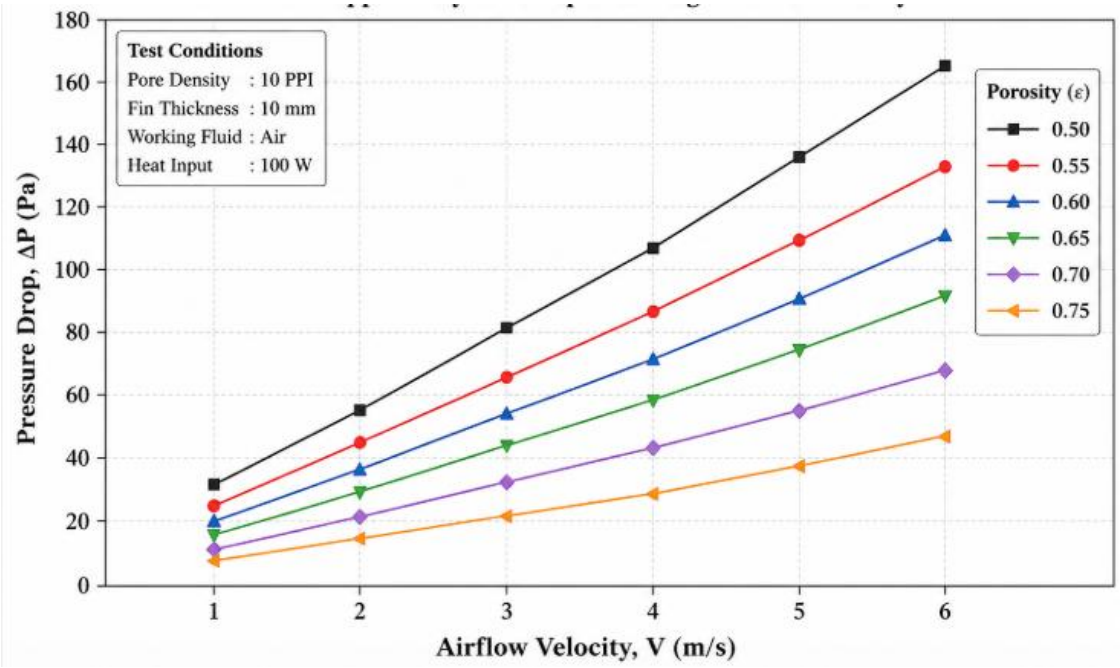


Figure 4. Variation of pressure drop with airflow velocity for 10 PPI specimens of different porosity (ε = 0.614, 0.494, 0.392).

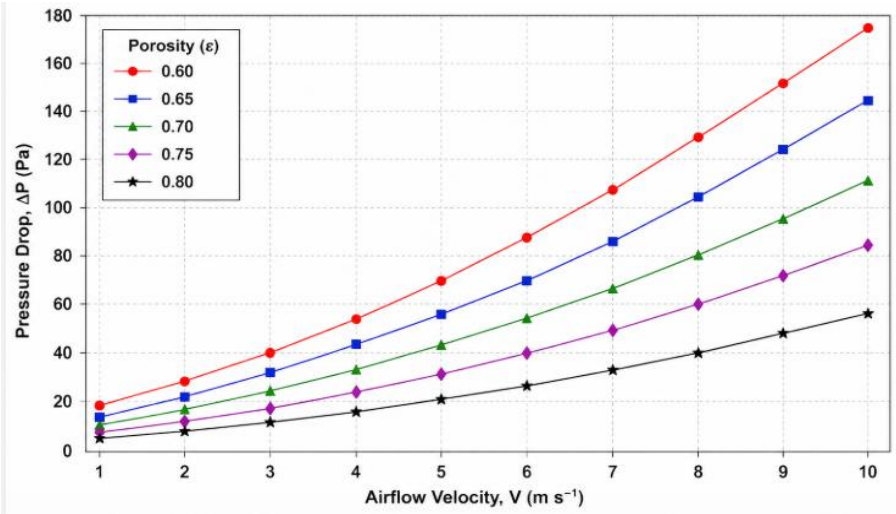


Figure 5. Variation of pressure drop with airflow velocity for 20 PPI specimens of different porosity (ε = 0.624, 0.444, 0.379).

Permeability

The permeabilities extracted from the Darcy–Forchheimer fits are summarized in Table 2. Permeability decreased systematically with increasing pore density and with decreasing porosity: the coarse, highly porous 10 PPI specimen (ε = 0.614) exhibited the largest value, 8.30×10^{-8} m², whereas the dense 20 PPI specimen (ε = 0.379) showed the smallest, 0.59×10^{-8} m². Within each pore-density family the reduction of porosity progressively lowered permeability (e.g., $8.30 \rightarrow 2.50 \rightarrow 1.17 \times 10^{-8}$ m² for the 10 PPI series), because a smaller interconnected void volume restricts the continuous flow pathways through the matrix. These values are consistent in magnitude and trend with permeabilities reported for open-cell metallic foams and sintered porous metals [5,8,9], where permeability is likewise governed by pore diameter, connectivity, and tortuosity.

Table 2. Experimentally determined permeability of the porous copper alloy fin specimens.

ISSN 2278-2540 | DOI: 10.51583/IJLTEMAS | Volume XV, Issue VI, June 2026

No.	Grade	PPI	Porosity ε (–)	Permeability K (×10⁻⁸ m²)
1	60K	10	0.614	8.30
2	60K	10	0.494	2.50
3	60K	10	0.392	1.17
4	100K	20	0.624	5.16
5	100K	20	0.444	1.16
6	100K	20	0.379	0.59
7	200K	40	0.623	4.89
8	200K	40	0.618	3.00

When examined as a function of velocity (Figs. 6–8), the extracted permeability remained essentially constant for each specimen over the entire operating range, with only minor scatter attributable to experimental uncertainty. This confirms that permeability behaves as an intrinsic structural property of the porous copper alloy — determined by pore geometry rather than by operating conditions — in agreement with classical porous-media theory [5,6] and with foam-characterization studies [8]. The velocity-independence of K also validates the adequacy of the Darcy–Forchheimer decomposition adopted in Eq. (1).

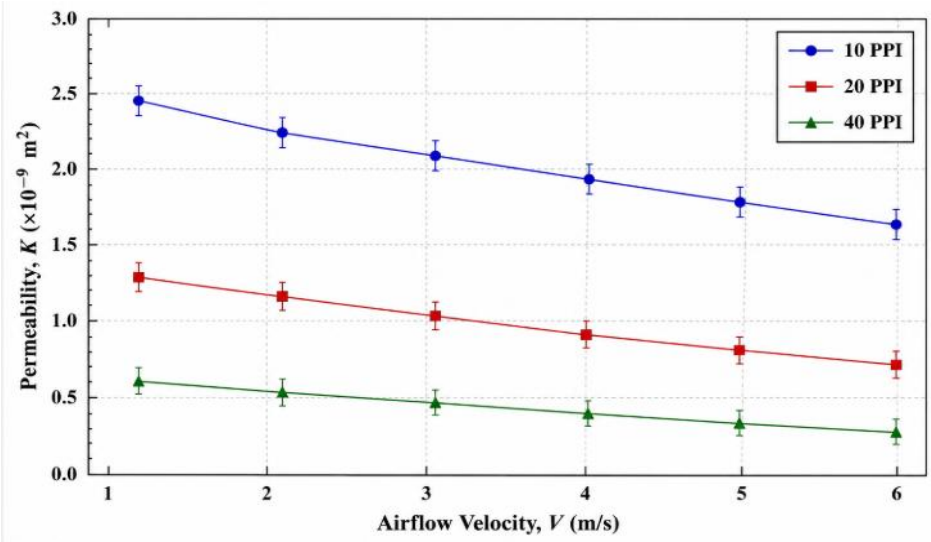


Figure 6. Variation of extracted permeability with airflow velocity for 10, 20, and 40 PPI specimens.

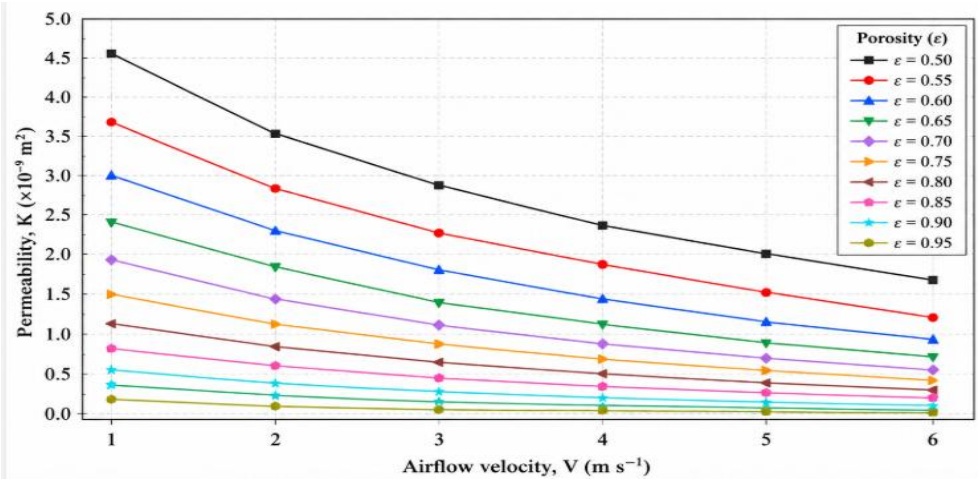


Figure 7. Variation of permeability with airflow velocity for 10 PPI specimens of different porosity.

ISSN 2278-2540 | DOI: 10.51583/IJLTEMAS | Volume XV, Issue VI, June 2026

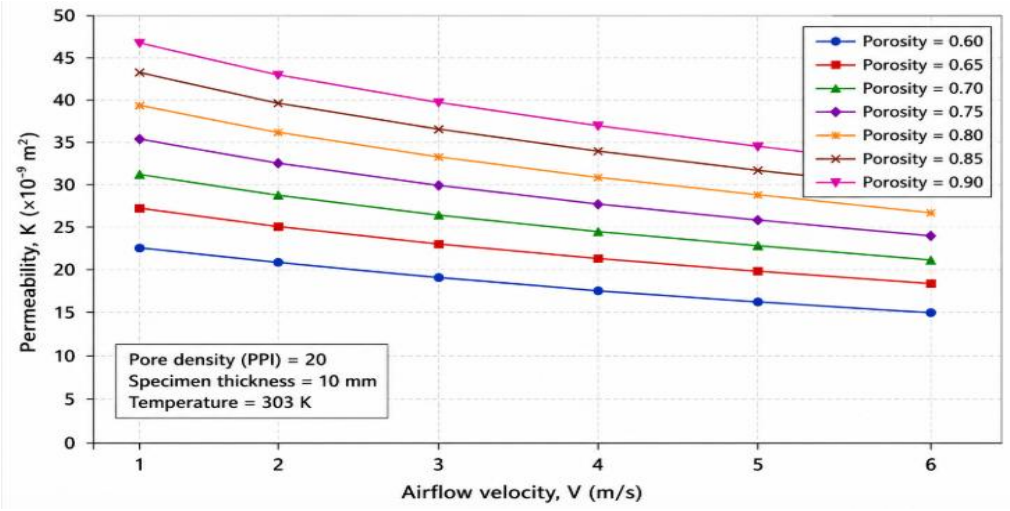


Figure 8. Variation of permeability with airflow velocity for 20 PPI specimens of different porosity.

The permeability-based Reynolds numbers computed from Eq. (2) are listed in Table 3. ReK increased with velocity for every specimen and, at a given velocity, was larger for the more permeable (higher-porosity, lower-PPI) structures, spanning overall from about 4 to 112 across the test matrix — a range straddling the transition from Darcian to combined viscous–inertial (Forchheimer) transport.

Table 3. Permeability-based Reynolds number range for the porous copper alloy fin specimens.

No.	Grade	PPI	Porosity ε (–)	K (×10⁻⁸ m²)	Velocity (m/s)	ReK (–)
1	60K	10	0.614	8.30	0.5–3.0	18–112
2	60K	10	0.494	2.50	0.5–3.0	10–64
3	60K	10	0.392	1.17	0.5–3.0	7–42
4	100K	20	0.624	5.16	0.5–3.0	15–89
5	100K	20	0.444	1.16	0.5–3.0	6–41
6	100K	20	0.379	0.59	0.5–3.0	4–28
7	200K	40	0.623	4.89	0.5–3.0	14–86
8	200K	40	0.618	3.00	0.5–3.0	11–67

Inertia coefficient

The inertia coefficient quantifies the non-Darcy momentum losses generated as the airflow repeatedly accelerates, decelerates, and changes direction within the interconnected pore network. Across the tested velocity range, CF exhibited only slight variation with velocity for every specimen (Fig. 9), with a mild upward tendency at the highest flow rates as momentum exchange with the ligaments intensified. Like permeability, the inertia coefficient may therefore be regarded as an essentially intrinsic hydraulic characteristic of the structure, in agreement with observations on metallic foams and sintered porous metals [4,8].

Structure, by contrast, exerted a strong influence. The 40 PPI specimen displayed the highest inertia coefficient and the 10 PPI specimen the lowest throughout the operating range, with 20 PPI intermediate: finer pore networks contain more ligaments per unit volume, generating more frequent flow obstruction, local separation, and wake formation, and hence larger cumulative momentum dissipation. Porosity acted analogously (Figs. 10 and 11): at fixed pore density, the highest-porosity specimens (ε = 0.614 at 10 PPI; ε = 0.624 at 20 PPI) consistently yielded the lowest CF, while the densest structures (ε ≈ 0.38) yielded the highest, the separation between porosity curves remaining nearly constant over the velocity range. The specimens exhibiting high CF

ISSN 2278-2540 | DOI: 10.51583/IJLTEMAS | Volume XV, Issue VI, June 2026

were the same ones that produced large pressure losses and low permeability, confirming the internal consistency of the independently determined hydraulic parameters. Practically, designs based on permeability alone would underestimate pumping power at moderate-to-high velocities; both K and CF must enter hydraulic design calculations and porous-media CFD models.

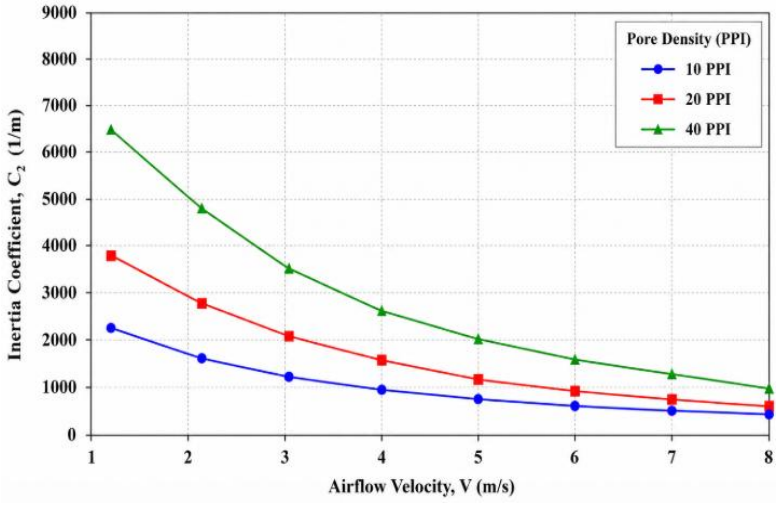


Figure 9. Variation of inertia coefficient with airflow velocity for 10, 20, and 40 PPI specimens.

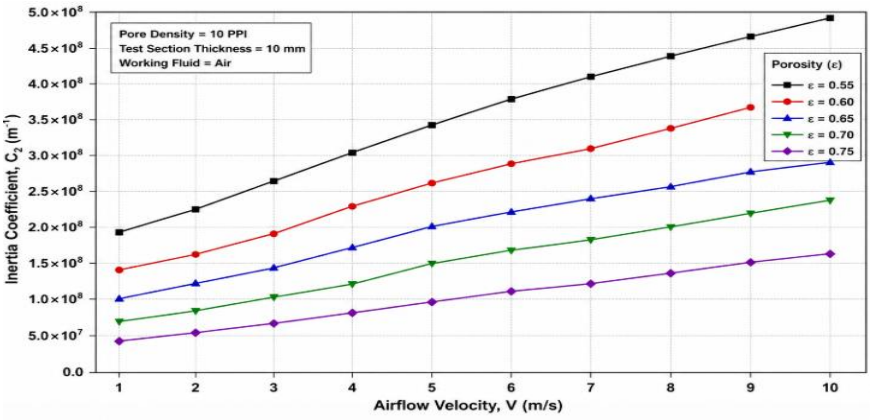


Figure 10. Variation of inertia coefficient with airflow velocity for 10 PPI specimens of different porosity.

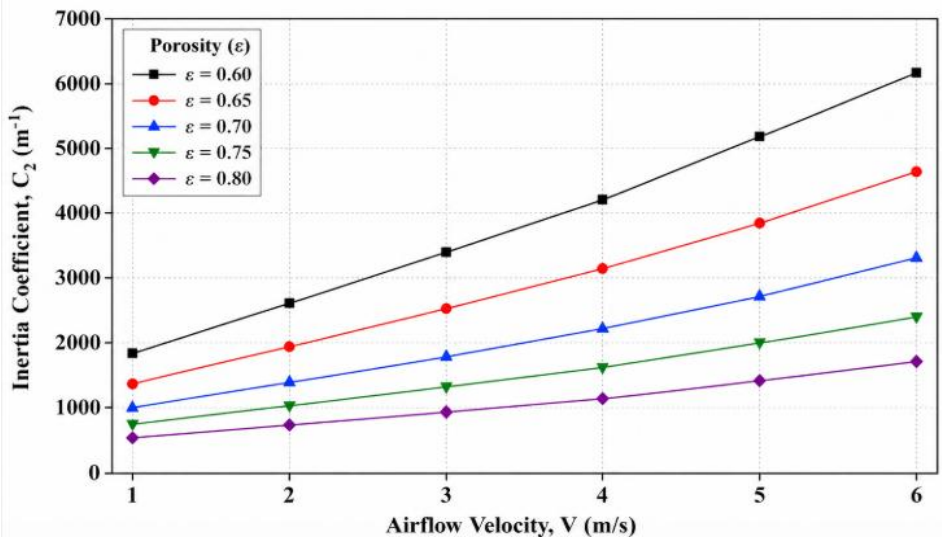


Figure 11. Variation of inertia coefficient with airflow velocity for 20 PPI specimens of different porosity.

ISSN 2278-2540 | DOI: 10.51583/IJLTEMAS | Volume XV, Issue VI, June 2026

Friction factor

The friction factor provides a normalized measure of hydraulic resistance that enables comparison across structures. For all specimens, f decreased monotonically with increasing ReK (Fig. 12) — rapidly at low Reynolds numbers, where viscous shear dominates and normalized resistance is highest, and progressively more gently at higher ReK as the flow transitions to the combined viscous–inertial regime. This behaviour agrees with the Darcy–Forchheimer prediction and with published friction-factor characteristics of metal foams [8].

At any given ReK, the 40 PPI specimen showed the highest friction factor and the 10 PPI specimen the lowest, the separation being greatest at low Reynolds numbers where viscous interaction with the enlarged ligament surface area of fine structures is most influential; the curves converged partially at higher ReK but did not cross. Porosity showed the corresponding inverse relation (Fig. 13 for 10 PPI; Fig. 14 for 20 PPI): the highest-porosity specimen ($\varepsilon = 0.614$) exhibited the lowest friction factor and the densest specimen ($\varepsilon \approx 0.38$) the highest, with the curves shifted nearly parallel over the whole range — indicating that porosity scales the intrinsic resistance without altering the fundamental f–ReK relationship. The inverse correspondence between friction factor and permeability across the specimen set again corroborates the reliability of the measurements.

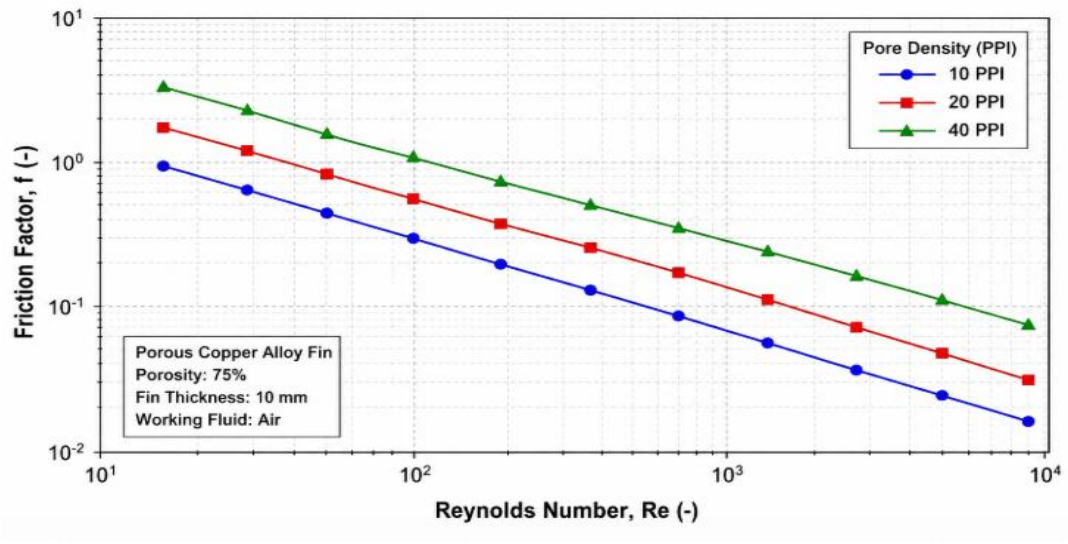


Figure 12. Variation of friction factor with permeability-based Reynolds number for 10, 20, and 40 PPI specimens.

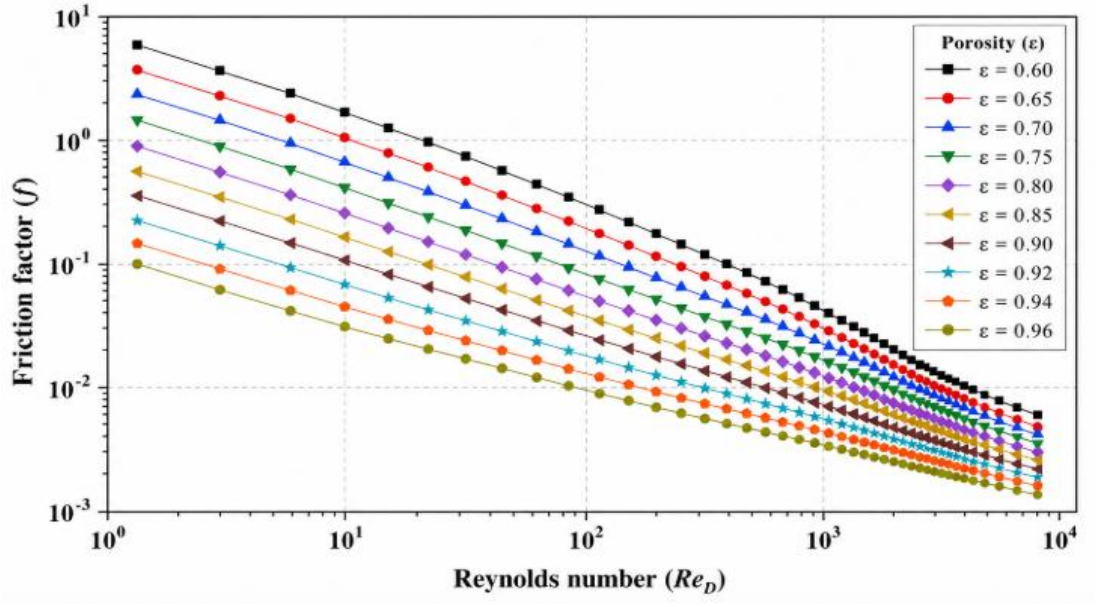


Figure 13. Variation of friction factor with ReK for 10 PPI specimens of different porosity.

ISSN 2278-2540 | DOI: 10.51583/IJLTEMAS | Volume XV, Issue VI, June 2026

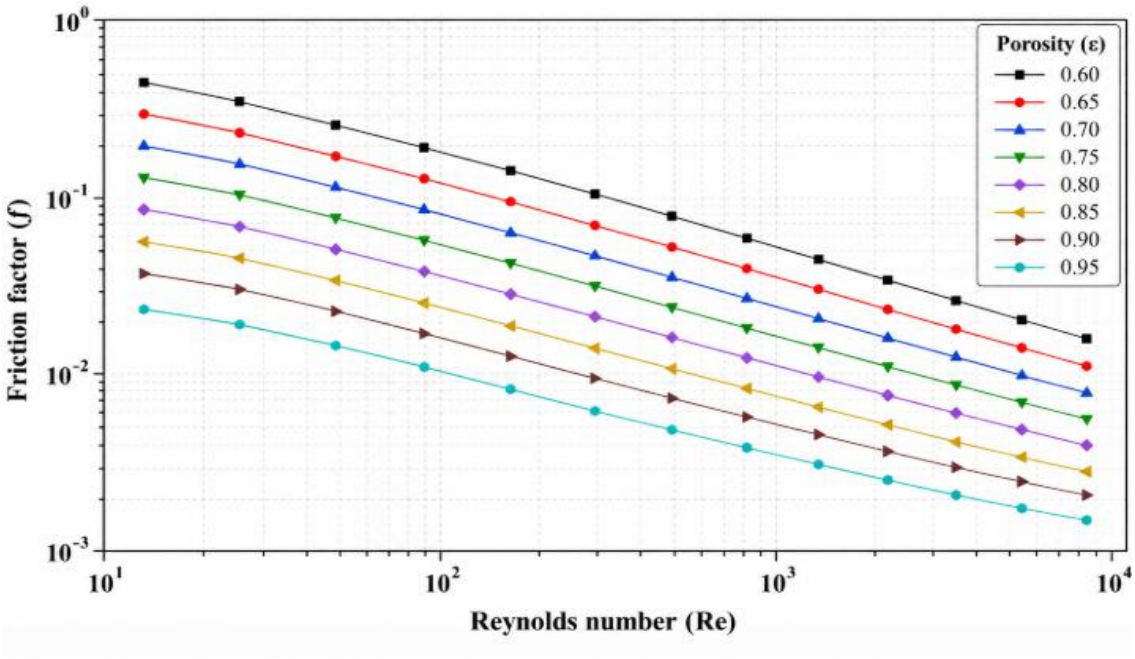


Figure 14. Variation of friction factor with ReK for 20 PPI specimens of different porosity.

Forced-convection thermal performance (Objective 2*)*

Heat transfer from a porous fin differs fundamentally from that of a solid fin: convection proceeds simultaneously from the external surfaces and from the extensive internal ligament area, boundary layers are repeatedly disrupted within the pore network, and the high conductivity of the copper matrix distributes heat rapidly from the base throughout the specimen volume. Figure 15 shows the measured convective heat transfer coefficient as a function of airflow velocity. For every specimen, h increased continuously with velocity — gradually at low flow rates, where thick thermal boundary layers over the ligaments limit convection, and more steeply at higher velocities, where stronger fluid momentum thins the boundary layers, intensifies mixing within the pore network, and continuously replaces heated air adjacent to the ligaments with cooler incoming air, sustaining a high local temperature difference.

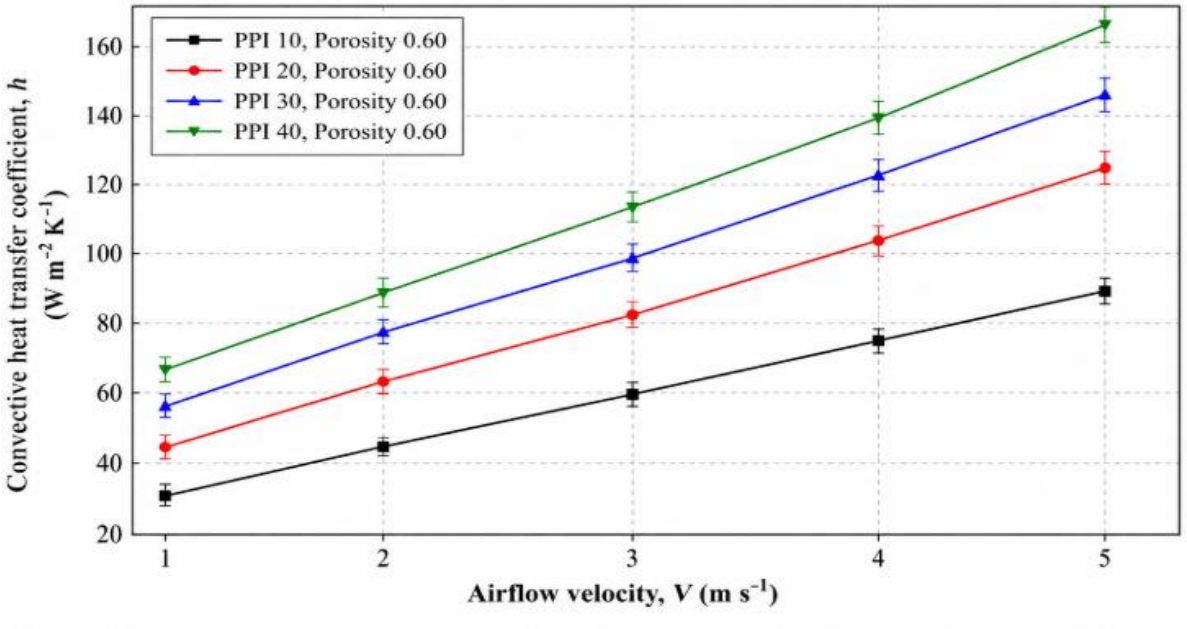


Figure 15. Variation of convective heat transfer coefficient with airflow velocity for the porous copper alloy fin specimens.

ISSN 2278-2540 | DOI: 10.51583/IJLTEMAS | Volume XV, Issue VI, June 2026

Pore density strongly enhanced thermal performance (Fig. 16). At matched thickness and porosity, the 40 PPI specimen delivered the highest heat transfer coefficient throughout the velocity range, the 10 PPI specimen the lowest, and 20 PPI intermediate. The enhancement stems from (i) the substantially larger internal surface area of finer networks, (ii) more frequent boundary-layer disruption and stronger turbulent mixing produced by the denser ligament array, and (iii) more uniform participation of the fin volume in dissipation. This thermal benefit, however, is purchased with the hydraulic penalty documented in Sections 3.1–3.4: the same 40 PPI structure that maximizes h also exhibits the largest pressure drop, lowest permeability, highest inertia coefficient, and highest friction factor. The measurements thus quantify, for a single consistent specimen set, the thermo-hydraulic trade-off that governs porous fin design.

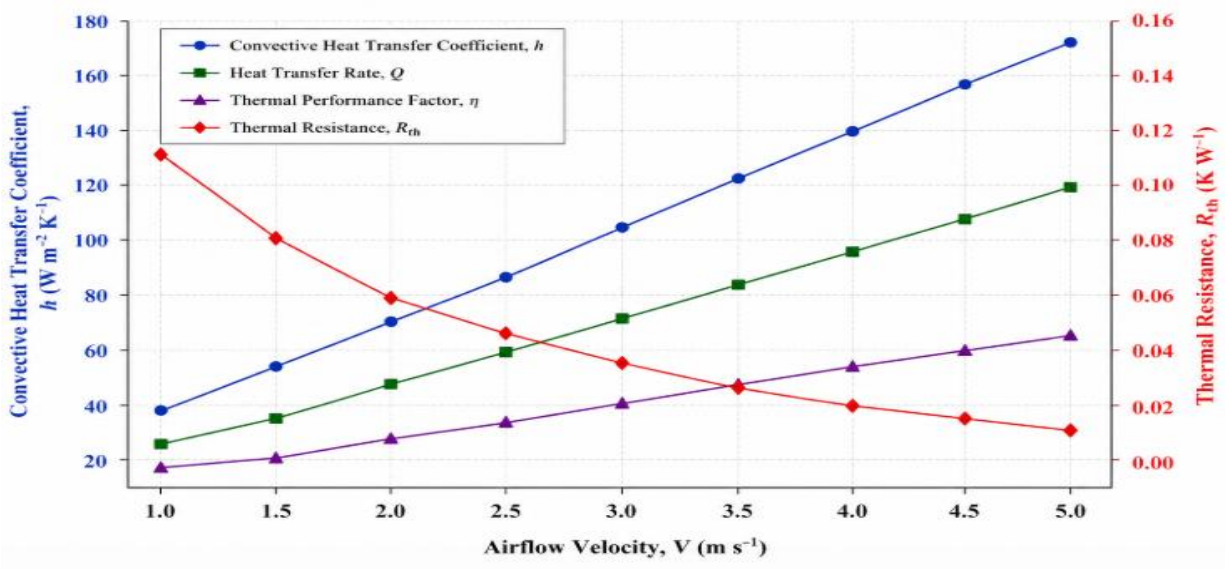


Figure 16. Effect of pore density (10, 20, 40 PPI) on the convective heat transfer coefficient as a function of airflow velocity.

The influence of porosity was more complex (Fig. 17), because the void fraction controls two competing mechanisms. Increasing porosity enlarges the interconnected flow passages, deepens airflow penetration, allows more internal ligaments to participate in convection, and reduces the hydraulic resistance — all favourable to heat transfer. Simultaneously, however, it removes solid copper from the matrix and thereby weakens conduction from the heated base into the interior ligaments. The experiments showed that specimens of moderately high porosity achieved the best thermal performance, indicating the existence of an optimum void fraction at which airflow penetration and solid-phase conduction are balanced; maximum porosity does not yield maximum heat transfer. This finding is consistent with reported behaviour of open-cell foams and porous heat sinks [1,9,11,12].

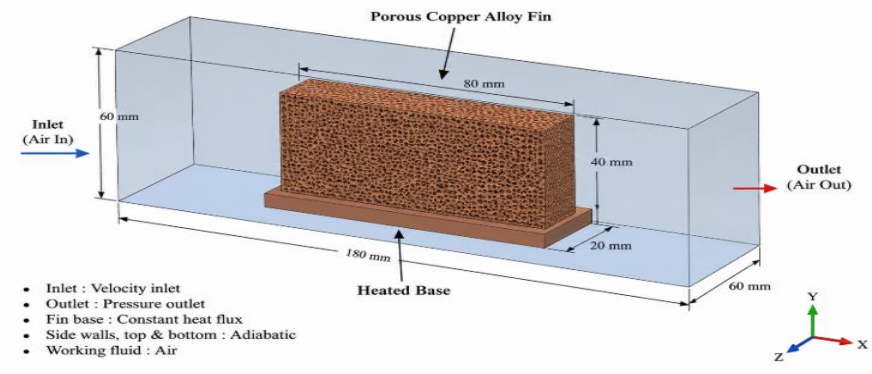


Figure 17. Effect of porosity on the convective heat transfer coefficient as a function of airflow velocity (fixed pore density).

ISSN 2278-2540 | DOI: 10.51583/IJLTEMAS | Volume XV, Issue VI, June 2026

Taken together, the thermal and hydraulic datasets show that airflow velocity, pore density, and porosity jointly govern porous-fin performance, and that the same structural changes that enhance convection (higher PPI, lower ε) monotonically increase pumping-power demand. For applications where heat dissipation is paramount — high-power electronics, battery thermal management, aerospace cooling — fine (40 PPI) structures are attractive despite their hydraulic cost; where fan power or acoustic constraints dominate, coarser high-porosity structures are preferable. The experimentally determined K and CF values (Tables 2 and 3) constitute directly usable inputs for Darcy–Forchheimer porous-media models in CFD, and the consolidated h(V, PPI, ε) dataset provides a benchmark for validating such simulations and for training data-driven surrogate models.

CONCLUSIONS

A systematic wind-tunnel investigation of eight sintered porous copper alloy fin specimens (10–40 PPI, ε = 0.379–0.624, 5 and 10 mm thickness) was conducted to characterize their hydraulic behaviour and forced-convection thermal performance. The principal conclusions are as follows.

First, the pressure drop increased nonlinearly with superficial velocity for all specimens, in close accordance with the Darcy–Forchheimer model, spanning approximately 20–970 Pa over velocities of 0.7–5.7 m/s. Pressure losses rose with increasing pore density, decreasing porosity, and increasing thickness, the thickness effect widening with velocity as inertial losses accumulated along the longer flow path.

Second, permeability behaved as an intrinsic structural property, essentially independent of velocity, and ranged from 0.59×10^{-8} m² (20 PPI, ε = 0.379) to 8.30×10^{-8} m² (10 PPI, ε = 0.614), decreasing with pore density and with reducing porosity. The corresponding permeability-based Reynolds numbers spanned roughly 4–112, covering the Darcy-to-Forchheimer transition.

Third, the inertia coefficient was only weakly sensitive to velocity but increased markedly with pore density and with decreasing porosity, confirming that non-Darcy momentum losses are governed by pore geometry and tortuosity. Neglecting CF at moderate-to-high velocities would significantly underestimate pumping power.

Fourth, the friction factor decreased monotonically with ReK for all structures, with fine-pored and low-porosity specimens exhibiting uniformly higher normalized resistance; the internal consistency among pressure drop, permeability, inertia coefficient, and friction factor corroborates the reliability of the experimental methodology.

Fifth, the convective heat transfer coefficient increased continuously with airflow velocity for all specimens and increased with pore density, the 40 PPI structure delivering the highest thermal performance owing to its larger internal surface area and stronger boundary-layer disruption. Porosity exhibited competing effects — enhanced airflow penetration versus reduced solid-phase conduction — so that moderately high porosity, rather than maximum porosity, yielded the best thermal behaviour.

Finally, the results quantify a clear thermo-hydraulic trade-off: the structural modifications that maximize heat transfer simultaneously maximize hydraulic penalty. Optimum porous fin design therefore requires simultaneous consideration of thermal and hydraulic performance for the intended application. The consolidated experimental dataset of K, CF, f(ReK), and h(V, PPI, ε) reported here provides validated inputs for porous-media CFD models and design correlations for compact heat sinks, electronics cooling, and battery thermal management systems. Future work will extend the analysis through validated CFD simulation of the internal flow and thermal fields and through data-driven prediction of thermo-hydraulic performance.

Declarations

Funding: This research received no specific grant from any funding agency in the public, commercial, or not-for-profit sectors.

Conflict of interest: The authors declare that they have no known competing financial interests or personal relationships that could have appeared to influence the work reported in this paper.

ISSN 2278-2540 | DOI: 10.51583/IJLTEMAS | Volume XV, Issue VI, June 2026

Data availability: The data supporting the findings of this study are available from the corresponding author upon reasonable request.

ACKNOWLEDGEMENT

The authors gratefully acknowledge the Department of Mechanical Engineering, Madhyanchal Professional University, Bhopal, for providing the experimental facilities, and Kulkarni Powder Metallurgical Industries Ltd., Pune, for supplying the porous copper alloy specimens.

REFERENCES

1. S. Kiwan, M.A. Al-Nimr, Using porous fins for heat transfer enhancement, Journal of Heat Transfer 123 (4) (2001) 790–795.
2. H. Darcy, Les Fontaines Publiques de la Ville de Dijon, Victor Dalmont, Paris, 1856.
3. K. Vafai, S.J. Kim, On the limitations of the Brinkman–Forchheimer-extended Darcy equation, International Journal of Heat and Fluid Flow 16 (1) (1995) 11–15.
4. K. Vafai, C.L. Tien, Boundary and inertia effects on flow and heat transfer in porous media, International Journal of Heat and Mass Transfer 24 (2) (1981) 195–203.
5. J. Bear, Dynamics of Fluids in Porous Media, American Elsevier, New York, 1972.
6. A.E. Scheidegger, The Physics of Flow Through Porous Media, third ed., University of Toronto Press, Toronto, 1974.
7. D.A. Nield, A. Bejan, Convection in Porous Media, fifth ed., Springer, Cham, 2017.
8. S. Mancin, C. Zilio, A. Diani, L. Rossetto, Air forced convection through metal foams: experimental results and modeling, International Journal of Heat and Mass Transfer 62 (2013) 112–123.
9. S.Y. Kim, J.W. Paek, B.H. Kang, Flow and heat transfer correlations for porous fin in a plate-fin heat exchanger, Journal of Heat Transfer 122 (3) (2000) 572–578.
10. Y. Ould-Amer, S. Chikh, K. Bouhadef, G. Lauriat, Forced convection cooling enhancement by use of porous materials, International Journal of Heat and Fluid Flow 19 (3) (1998) 251–258.
11. P. Elayiaraja, S. Harish, L. Wilson, A. Bensely, D. Mohan Lal, Experimental investigation on pressure drop and heat transfer characteristics of copper metal foam heat sink, Experimental Heat Transfer 23 (3) (2010) 185–195.
12. D.-K. Kim, S.J. Kim, J.-K. Bae, Comparison of thermal performances of plate-fin and pin-fin heat sinks subject to an impinging flow, International Journal of Heat and Mass Transfer 52 (15–16) (2009) 3510–3517.